Corrosion Science 158 (2019) 108103

Contents lists available at ScienceDirect

Corrosion Science

journal homepage: www.elsevier.com/locate/corsci

Microstructure and surface oxidation behavior of an austenitic Fe-Mn-Si-Cr-Ni-Co shape memory stainless steel at 800 °C in air

R. Silva[a,*], C. Arana[a], A.M. de Sousa Malafaia[b], A.A. Mendes Filho[c], C. Pascal[d], J. Otubo[e,f], V.L. Sordi[a], C.A.D. Rovere[a,*]

[a] Munir Rachid Corrosion Laboratory, Department of Materials Engineering, Federal University of São Carlos, Rodovia Washington Luis Km 235, 13565-905, São Carlos, SP, Brazil
[b] Department of Mechanical Engineering, Federal University of São João Del Rei, Praça Frei Orlando, 170, Centro, São João Del Rei, MG, 36307-352, Brazil
[c] Institute for Frontier Materials, Deakin University, Geelong, VIC, 3216, Australia
[d] University of Grenoble Alpes, CNRS, Grenoble INP, SIMaP, F-38000, Grenoble, France
[e] Division of Mechanical Engineering, Technological Institute of Aeronautics, Praça Marechal Eduardo Gomes, 50. Vila das Acácias, 12228-900, São José dos Campos, SP, Brazil
[f] Nuclear and Energy Research Institute - IPEN, 05508-000, São Paulo, SP, Brazil

ARTICLE INFO

Keywords:
Stainless steel
High temperature oxidation
Microstructure
SEM
TEM
Thermodynamic simulations

ABSTRACT

In the present research, the microstructure and oxidation behavior of an Fe-8.26Mn-5.25Si-12.80Cr-5.81Ni-11.84Co shape memory stainless steel (SMSS) was studied at 800 °C in air for up to 120 h. Phase changes and oxidation mechanism were discussed based on microscopy analyses, thermogravimetric measurements and thermodynamic simulations. The results show that oxidation exposure promotes the formation of the σ, χ and ferrite phases in the metallic substrate. The oxidation behavior follows a parabolic law, with the kinetics of oxidation being controlled by the Mn_2O_3 oxide growth in the first hours, and by Mn_3O_4 and $MnCr_2O_4$ spinel growth after 24 h of exposure.

1. Introduction

Austenitic stainless steels are widely utilized in the manufacturing and assembly of engineering structures to use in chemical and power generation industries, which involve exposure to high temperatures [1,2]. In such industrial applications, pipes and plates are generally joined by welding, which, depending on the adopted procedures, may impair the performance of the final assembled structure [3]. Given this potential structural risk, austenitic FeMnSiCrNi shape memory stainless steel (SMSS) arises as an alternative material for joining pipes and plates. This new class of materials combines remarkable properties such as shape memory effect (SME), good corrosion resistance, excellent mechanical properties and ease of fabrication that can be used by industries to significantly improve the functionality and durability of their assembled structures [2,4–6]. According to Dai et al. [7] and Li et al. [8], the SME exhibited by austenitic FeMnSiCrNi SMSSs can be a successful economic alternative to conventional welding pipe coupling processes. Thus, parts of a given structure or component (used in chemical or power generation industries) can be joined by the SME of FeMnSiCrNi SMSS at room temperature, and subsequently, the assembled engineering structure could be used in high temperature environments. Therefore, there needs to be an-depth understanding of the behavior of these FeMnSiCrNi SMSSs at high temperatures considering not only oxidation aspects but also microstructural features.

However, it has been reported that during high-temperature oxidation tests carried out for 100 h in air at 800 °C, that the high manganese (Mn) content present in the FeMnSiCrNi SMSSs causes a mass gain ten times greater than that of conventional austenitic AISI 304 [2]. According to literature [2,9,10], this inferior oxidation behavior is related to the formation of Mn oxides and Mn-Cr spinels, which exhibit rapid growth kinetics and are much less protective than a chromium (III) oxide [chromia (Cr_2O_3)] layer [11].

Since Mn is an essential alloying element for the SME of SMSSs [12], more research should be performed in order to verify other possible alloying element combinations that have lower Mn contents with the intention of improving oxidation resistance without causing a loss to the SME. Thus, the Fe-8.26Mn-5.25Si-12.8Cr-5.81Ni-11.84Co SMSS can be an alternative for use in high temperatures because of its lower Mn content and higher chromium (Cr) content compared to that of conventional Fe-14Mn-5Si-9Cr-5Ni. Furthermore, literature shows [13]

* Corresponding authors.
E-mail addresses: rsilvacorr@gmail.com (R. Silva), rovere@ufscar.br (C.A.D. Rovere).

https://doi.org/10.1016/j.corsci.2019.108103
Received 23 February 2019; Received in revised form 5 July 2019; Accepted 14 July 2019
Available online 19 July 2019
0010-938X/

Table 1
Alloy chemical composition (wt.%).

Material	C	Mn	Si	Cr	Ni	Co	Fe
FeMnSiCrNiCo	0.009	8.26	5.25	12.80	5.81	11.84	Bal.

that adding Cobalt (Co) to FeMnSiCrNi SMSSs promotes a decrease in the stacking fault energy, which is a necessary condition for the desired improvements to the SME. Nonetheless, very little information is available about the microstructural evolution and oxidation behavior of this new alloy at high temperatures. Therefore, this study aims to assess the microstructure and oxidation behavior of a Fe-8.26Mn-5.25Si-12.8Cr-5.81Ni-11.84Co SMSS at 800 °C for up to 120 h of oxidation in air, by means of thermogravimetric measurements, optical microscopy (OM), scanning electron microscopy (SEM), transmission electron microscopy (TEM) and X-ray diffraction (XRD) analyses.

2. Experimental procedure

The studied alloy was melted in a vacuum induction furnace (VIM), using high purity iron (Fe), silicon (Si), nickel (Ni), Mn, Cr, and Co. After melting the alloy, the ingot was first forged at 1280 °C into the shape of a bar, then it was solution treated for 1 h at 1050 °C and finally it was quenched in water at room temperature. Table 1 shows the chemical composition of the studied material obtained by inductively coupled plasma optical emission spectrometry (ICP-OES). Carbon (C) was determined by pyrolysis using a LECO CS-444. Cylindrical samples were cut to a 6 mm diameter and a 10 mm height through electrical discharge machining (EDM). After cutting, they were ground to 1200 grit with SiC abrasive paper, then measured and finally degreased with acetone.

Oxidation tests were performed in static air at 800 °C for the exposure periods of 5, 10, 24, 48, 72, 96 and 120 h. The temperature was chosen based on literature, which has shown that the temperature limit for air exposure in Fe-Cr alloys containing up to 13 wt.% Cr is around 800 °C [14]. Furthermore, studies show that austenitic steels have good oxidation resistance when exposed to temperatures below 850 °C [15,16]. The samples were individually placed into casted alumina crucibles to avoid mass losses generated by possible spallation of the formed oxides. After the various exposure times, the crucibles and samples were taken out of the furnace and cooled down to room temperature air. The mean and standard deviation values of the weight gain curve were calculated based on the two oxidation tests of each sample.

After oxidation tests, samples were cross-sectioned, mounted in cold cure polyester resin, ground to 1200 grit with SiC abrasive paper, and polished with a 1 µm alumina suspension. Subsequently, they were etched with Vilella's reagent (5 mL 37% HCl + 95 mL ethanol + 1 g picric acid), and also electrochemically etched with 10% oxalic acid solution by applying a current density of 1 A/cm^2 for 90 s. The indicated electrochemical etching process using the oxalic acid solution is known to preferentially attack Cr-rich regions that may be formed when austenitic steels are exposed to high temperatures [17,18]. The resulting microstructures were first examined by means of OM and then analyzed in a FEI Magellan 400 L SEM with an energy-dispersive X-ray spectroscopy (EDS) system.

In addition, TEM analyses in a FEI Tecnai F20 FEG microscope operating at 200 kV were performed on the microstructure of the sample oxidized for 120 h. The TEM foils were prepared using the focused ion beam (FIB) in-situ lift-out technique, with a FEI QUANTA 3D FEG SEM. EDS in TEM was used for detecting the microchemical composition of the sample. TEM site-specific sample preparation was used to directly observe the precipitation inside the grain.

The constituent phases within the microstructure of the solution-treated samples oxidized for 120 h were then characterized by X-ray diffraction (XRD), operated with Cu Kα at 50 kV and 100 mA, a scanning angle (2θ) between 20° and 100° and a scanning speed of 2°/min. Additionally, the oxide layers formed for up to 120 h were characterized by XRD.

Finally, the phase changes and oxidation mechanism of the alloy at 800 °C were addressed based on the thermodynamic stability of the phases predicted by Thermo-Calc software using the TCFE7 database [19,20].

3. Results and discussion

3.1. Microstructural characterization

Fig. 1(a) shows an optical micrograph representing the solution-treated sample. The matrix structure is basically composed of austenitic grains (represented by twins) and martensite-ε blocks generated during sample preparation. Fig. 1(b) shows the XRD pattern of the solution-treated sample, in which the presence of austenite and martensite-ε phases are confirmed. Kajiwara [21], Maji et al. [22] and Della Rovere et al. [23] also observed similar microstructures in Fe-Mn-Si-Cr-Ni SMSSs.

Fig. 2(a)–(g) shows SEM micrographs of the samples oxidized for 5, 10, 24, 48, 72, 96 and 120 h. During the oxidation process, the formation of a new phase in the structure of the material can be observed, which initially and preferably precipitates at grain boundaries, and then becomes generalized throughout the matrix as the oxidation exposure time reaches 120 h. According to the EDS composition analysis [Fig. 2(h)], these precipitates are enriched by Mn, Si, Cr and Ni.

The XRD pattern performed on the microstructure (metallic matrix)

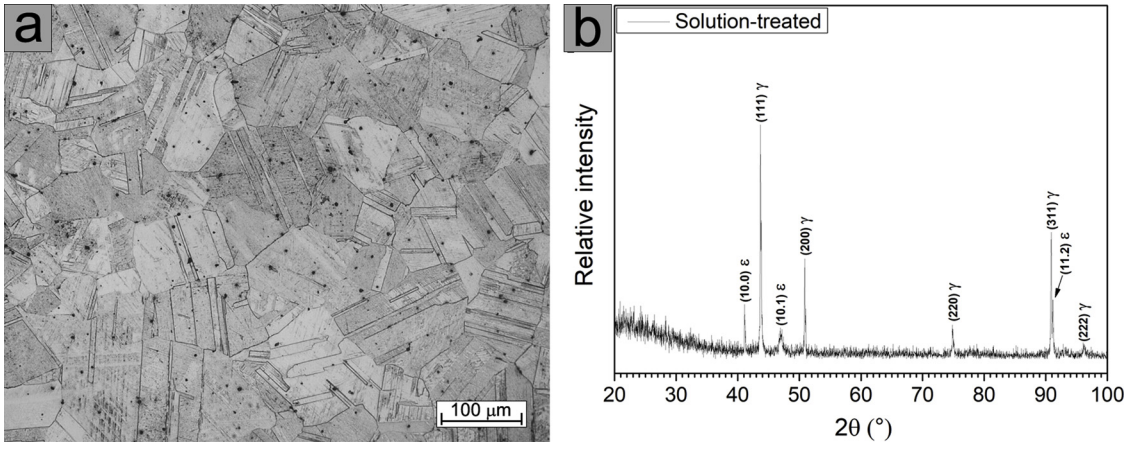

Fig. 1. Optical micrograph (a) and XRD pattern (b) of the microstructure of the solution-treated sample.

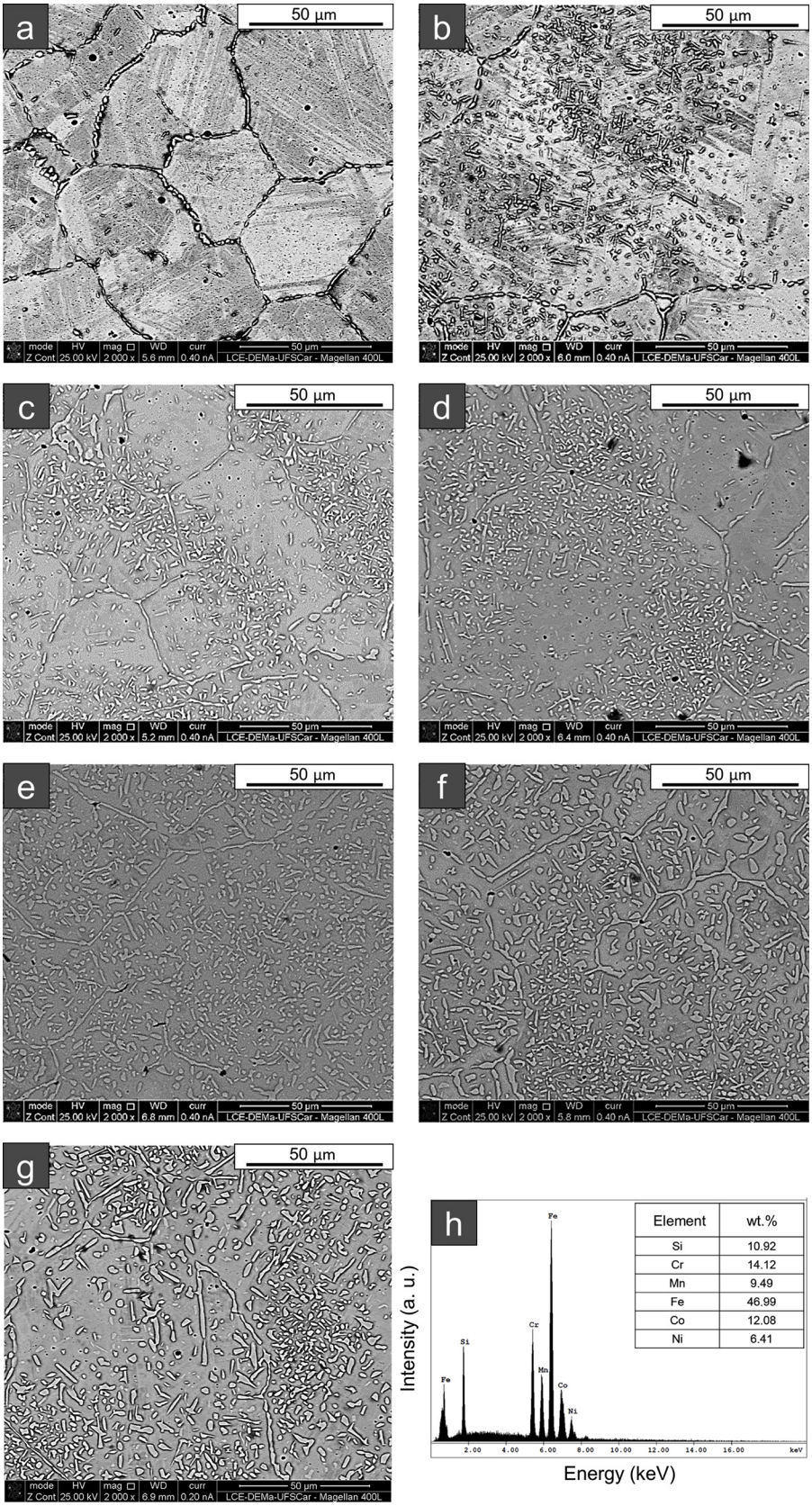

Fig. 2. SEM micrographs of the samples oxidized for 5 (a), 10 (b), 24 (c), 48 (d), 72 (e), 96 (f) and 120 h (g). EDS pattern of precipitates formed in the sample oxidized for 120 h (h).

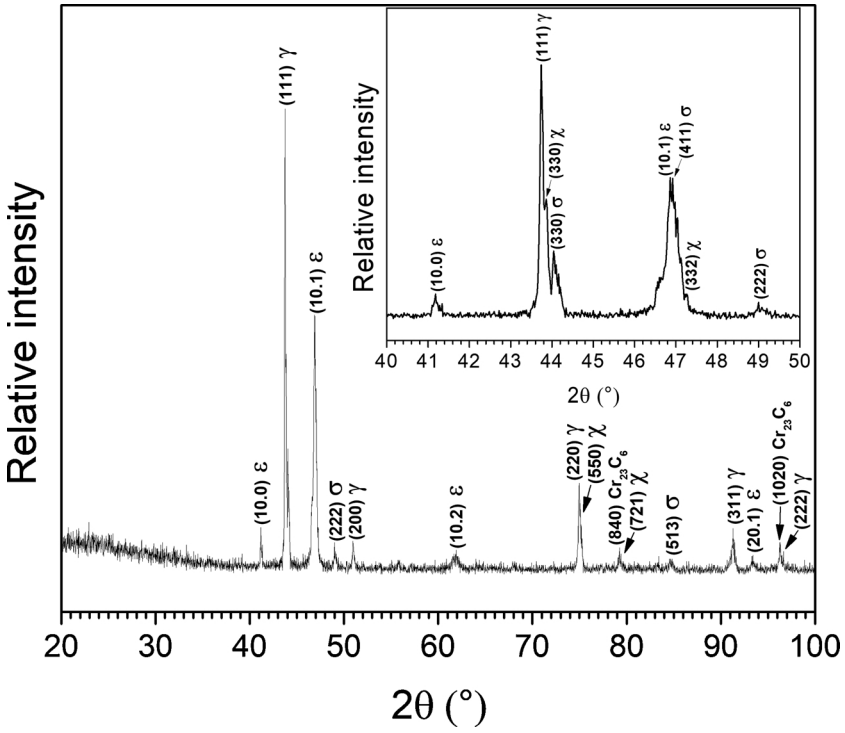

Fig. 3. XRD pattern of the alloy microstructure oxidized for 120 h.

of the sample oxidized for 120 h (Fig. 3) reveals characteristic peaks of the Sigma-phase (σ – JCPDS 05-0708), Cr carbides ($Cr_{23}C_6$ – JCPDS 35-0783) and Chi-phase (χ – JCPDS 31-0401). A plausible explanation for these results is as follows: (i) although the σ-phase formation in the studied alloy may be hindered by the presence of Ni and Co [18,24], its high Si content (above 2.5 wt.%) accelerates the σ-phase formation process [6,25]; (ii) $Cr_{23}C_6$ precipitation can occur in austenitic stainless steels when they are exposed to temperatures ranging from 500 °C to 900 °C [26,27]. Despite the fact that the C content in this Fe-Mn-Si-Cr-Ni-Co alloy is very low, the $Cr_{23}C_6$ precipitation is favored by the extensive exposure periods at 800 °C; (iii) the χ-phase precipitation has already been reported in Fe-Mn-Si-based SMSSs at high temperatures; however, the formation mechanism in these alloys remains unclear [2,28,29]. With regards to conventional stainless steels, the precipitation of χ-phase has been associated with the σ-phase formation as a result of thermal aging. According to literature, the χ-phase is an intermetallic compound formed in the steel structure before the σ-phase, being consumed as the precipitation of the σ-phase evolves [30,31].

TEM was used to further analyze the structural details of the studied alloy. Fig. 4 shows TEM images of the microstructure (metallic matrix) of the sample oxidized for 120 h, where the presence of two different types of precipitates can be observed inside the grains. Elemental mapping and chemical composition of these precipitates through EDS (Table 2) show that one is enriched by Mn and Cr, and the other is enriched by Mn, Si, Cr and Ni. Diffraction patterns performed on the precipitates enriched by Mn and Cr confirmed that they are from the σ-phase (tetragonal phase, which has lattice parameters of a = 8.86 Å and c = 4.61 Å) [32]. On the other hand, the precipitates enriched by Mn, Si, Cr and Ni were identified as a body-centered cubic (BCC) phase with a lattice parameter of 8.70 Å, which is consistent with the χ-phase. These results are in agreement with those reported by Stanford et al. [29], who observed a phase formation in the grain boundaries within the temperature range of 500 °C to 800 °C when investigating the stability of austenite in a number of FeMnSi-based SMSSs. By means of TEM analyses, Stanford et al. [29] verified that it was a χ-phase with BCC structure and a lattice parameter of 8.80 Å. Our finding also agrees with the recent study reported by Ma et al. [2], which observed the formation of the χ-phase enriched by Mn, Si, Cr and Ni in the grain boundaries and inside the metallic matrix when assessing the oxidation behavior of an Fe-14.26Mn-5.57Si-8.23Cr-4.96Ni SMSS at 800 °C.

3.2. Oxidation behavior

Fig. 5(a) shows the weight gain curve (per unit surface area) of the studied alloy as a function of the oxidation time at 800 °C in air. The weight gain obtained after 120 h of oxidation is approximately 0.68 mg/cm^2. This result shows that the studied alloy has an oxidation resistance more than four times greater than the alloy studied by Ma et al. [2], where a weight gain of 2.88 mg/cm^2 was observed after 100 h of isothermal oxidation at 800 °C. Additionally, the alloy in the current study presented better oxidation behavior than the alloy studied by Malafaia et al. [9] in approximately 100 h of cyclic oxidation at 800 °C (1.84 mg/cm^2). Nevertheless, it should be acknowledged that in the aforementioned studies, the alloys used were conventional FeMnSiCrNi, containing comparatively higher Mn contents and lower Cr contents than the presently studied FeMnSiCrNiCo SMSS, which are factors that influence the oxidation resistance of ferrous alloys [11]. Another aspect to consider is that the traditional AISI 304 isothermally oxidized at 800 °C for 100 h, gained around 0.23 mg/cm^2 [33], which is less than the studied material.

Fig. 5(a) shows that the general shape of the mass gain curve as a function of the oxidation time for the studied alloy appears to be parabolic. Thereby, weight gain square plots $(\Delta M/S)^2$ as a function of the oxidation time were performed. Fig. 5(b) shows the weight gain square, in which linearization as a function of oxidation time can be observed, proving that the oxidation kinetics of the FeMnSiCrNiCo SMSS is parabolic. When comparing the K_p values obtained in this research ($K_p = 3.64 \times 10^{-3}$ mg^2/cm^4.h) with those obtained by Ma et al. [2] ($K_p = 1.12 \times 10^{-1}$ mg^2/cm^4.h) and Malafaia et al. [9] ($K_p = 3.58 \times 10^{-2}$ mg^2/cm^4.h), the present results show that the oxidation rate of the studied alloy is much lower, which reveals that the FeMnSiCrNiCo SMSS alloy performs better at high temperatures.

Fig. 6(a–h) presents the cross-section of SEM images for samples oxidized between 5–120 h, respectively. Note that the oxide formed as a

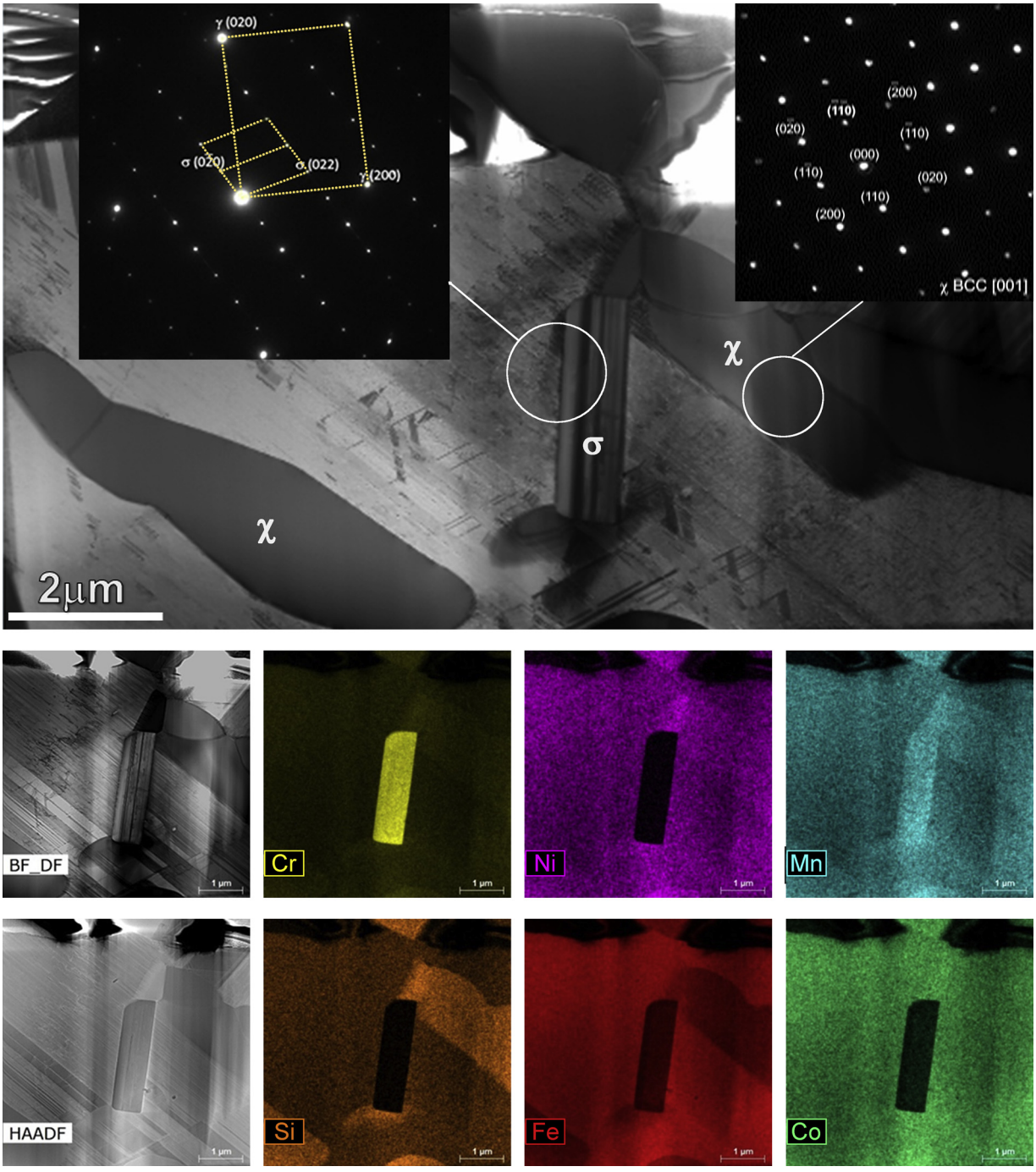

Fig. 4. TEM image and elemental mapping of the precipitates present inside the grains after 120 h of oxidation of the FeMnSiCrNiCo SMSS.

Table 2
EDS composition analyses (wt.%) of different matrix regions.

Material	Mn	Si	Cr	Ni	Co	Fe
σ-phase	7.12	0.10	67.60	0.08	1.85	23.25
χ-phase	10.47	9.73	15.68	7.82	14.39	41.91
Matrix close to precipitates	8.05	3.69	11.42	5.85	12.36	58.63

function of oxidation exposure presents a fairly irregular shape, displaying many recesses and thickness variations. The presence of a new phase located below the oxide layer that apparently has the same shape observed for the χ-phase in the grain boundaries (in the early stages of oxidation) can additionally be seen. However, the thickness of this phase increases with oxidation time. EDS analyses (Table 3) show that the composition of this phase is closer to that found in the metallic matrix, except for the Mn content, which decreases abruptly in the first 10 h of oxidation, and the Cr content that also decreases significantly after 24 h of oxidation.

Fig. 7 shows the cross-section SEM images of the sample oxidized for 120 h and its corresponding elemental mapping. The elemental mapping of the formed oxide layer shows that it is mainly composed of Mn and O which are evenly distributed throughout the oxide, and Cr which is mostly present at the metal/oxide interface. Although Fe is the major element of alloy, its oxides are significantly less stable than the oxides of other alloying elements (*i.e.*, Mn, Si and Cr). Thus, when Fe-Mn-Si-Cr-Ni-Co SMSS is thermally exposed at 800 °C, a selective

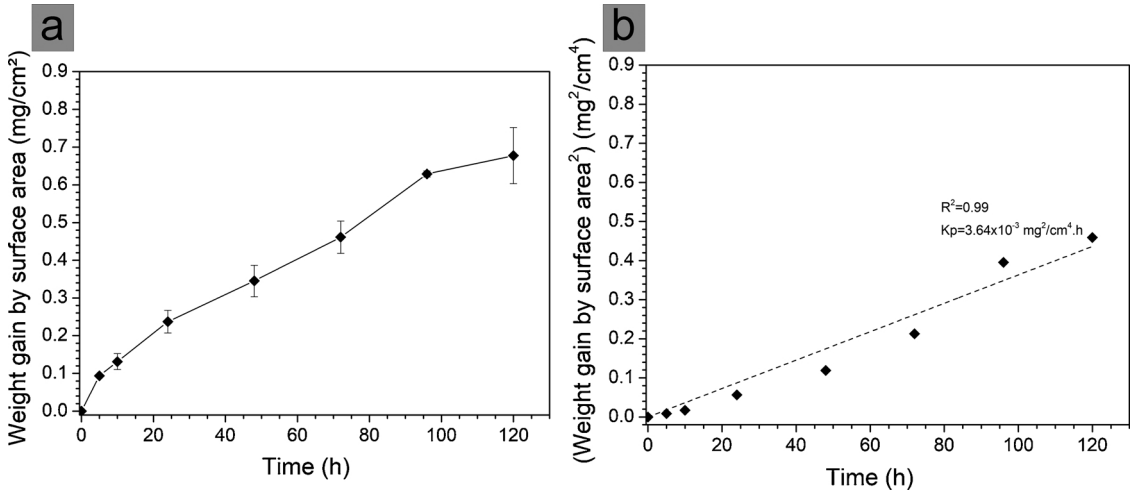

Fig. 5. Average weight gain curve (a) and square of the weight gain curve (b) of Fe-8.26Mn-5.25Si-12.8Cr-5.81Ni-11.84Co SMSS oxidized at 800 °C in air.

oxidation occurs in elements that form more stable oxides. However, through the elemental mapping, it is detectable that the formed oxide layer contains more Mn than Cr. This result is a consequence of the higher Mn diffusion through the first formed oxide layer, thus forming oxide on the surface of the material at a magnitude of almost two orders greater than that of Cr [34]. This fact explains the faster Mn-depletion with respect to the Cr in the layer located at the oxide/metal interface (Table 3). To characterize the (Mn,Cr)-depleted regions, the formed oxide layer after 120 h of oxidation was completely removed by grinding and the substrate surface was analyzed by XRD. The XRD patterns (Fig. 8) reveal that the (Mn,Cr)-depleted regions are ferrite (α-JCPDS 06-0696). This result is caused by the preferential oxidation of Mn (austenite stabilizer), generating the formation of Mn-depleted regions. In previous research this phenomena was considered responsible

Table 3
EDS chemical composition as a function of oxidation exposure of the phase formed at the oxide/metal interface.

Element weight (wt.%)						
Time (h)	Fe	Mn	Si	Cr	Ni	Co
5	42.47	5.54	7.12	12.85	6.84	12.01
10	51.96	2.65	6.98	13.13	7.28	13.72
24	50.03	2.47	7.10	11.91	6.57	13.14
48	66.20	1.79	6.37	7.83	4.66	13.15
72	65.85	1.78	7.43	7.90	4.44	12.60
96	67.15	1.95	6.74	6.89	4.33	12.94
120	66.57	1.84	6.68	6.96	4.93	13.01

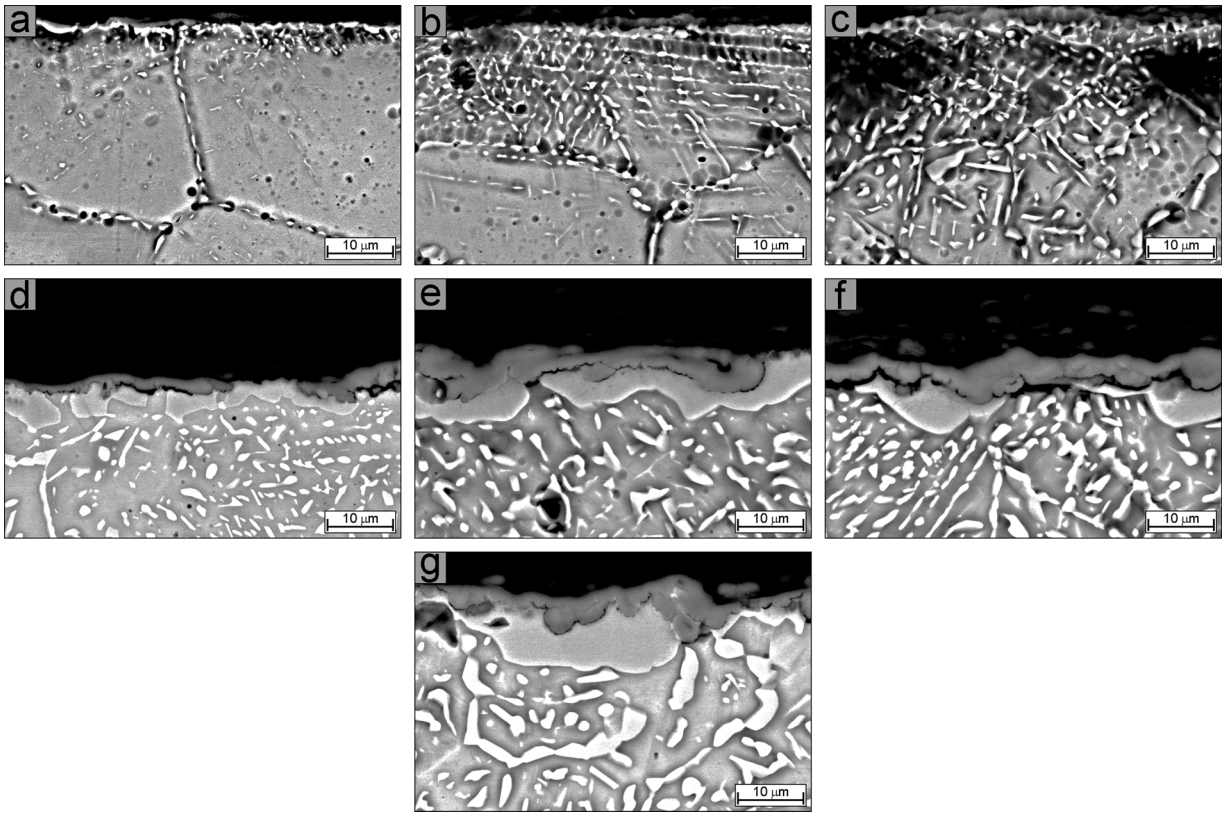

Fig. 6. Cross-section SEM images of oxidized samples for 5 (a), 10 (b), 24 (c), 48 (d), 72 (e), 96 (f) and 120 h (g).

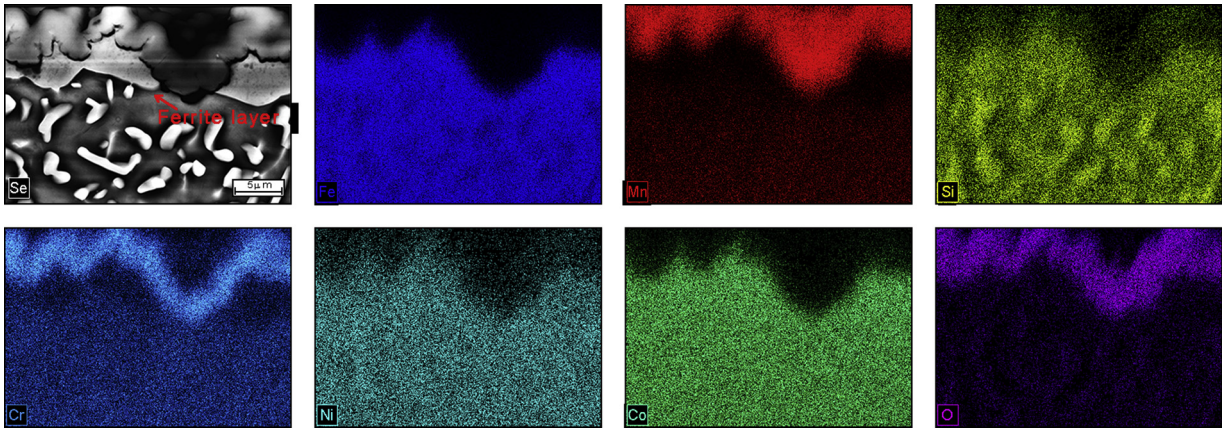

Fig. 7. Cross-sectional SEM image and corresponding elemental mapping of the sample oxidized for 120 h.

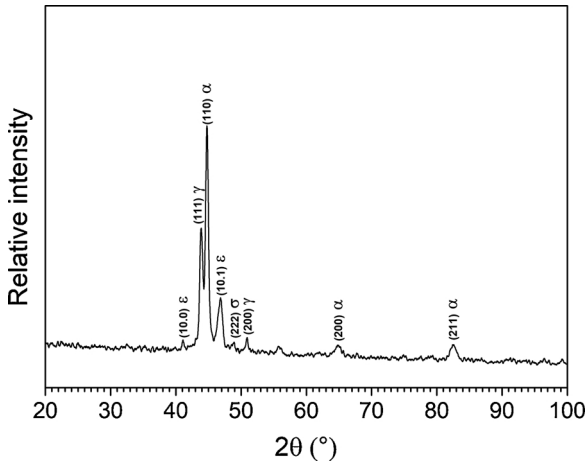

Fig. 8. XRD pattern of the sample oxidized for 120 h after grinding to completely remove all formed oxide.

for inducing the phase transformation from austenite to ferrite in these regions [2,9,35]. In addition, the (Mn,Cr)-depletion in the regions below the oxide layer is an indication that the growth of the oxide layer as a function of the oxidation time is controlled mainly by Mn and Cr cations diffusion throughout the oxide layer, as proposed by Wagner's theory for parabolic law [36].

Fig. 9(a) and (b) shows XRD patterns performed on the oxide layer of the samples oxidized for up to 120 h at 800 °C, where it can be seen that the oxide layer formed for up to 1 h of oxidation [Fig. 9(a)] is composed only of Mn_2O_3 (JCPDS 78-0390), it is also possible to observe χ-phase and α peaks. As the oxidation time increases [Fig. 9(b)], small peaks of Mn_3O_4 (JCPDS 80-0382) and $MnCr_2O_4$ spinel (JCPDS 75-1614) are observed, yet, the intensity of the peaks corresponding to the oxides of Mn_3O_4 and $MnCr_2O_4$ spinel become more pronounced after 24 h of oxidation. These results suggest that the kinetics of oxidation at the initial times of 0–24 h are primarily controlled by the growth of the Mn_2O_3 oxide, and after 24 h by the growth of the Mn_3O_4 and $MnCr_2O_4$ spinel. This behavior may be conceivable with parabolic law, where a higher oxidation rate is observed at the initial exposure times due to the less protective character of oxide composed (mainly of Mn), followed by a decrease in weight gain because of the formation and thickening of $MnCr_2O_4$ spinel. However, the oxidation rate at the initial times 0–24 h is lower than after 24 h, as observed at the weight gain curve [Fig. 5(a)]. This phenomenon has also been reported by Douglas et al. [37,38] during the beginning of the oxidation process of austenitic Fe-Mn-Cr stainless steels at high temperatures (700–1000 °C) and explained by the Mn volatilization. This is due to the fact that the oxide formed on the surface of the Fe-Mn-Si-Cr-Ni-Co-SMSS in the initial stages of the oxidation process is mainly composed by Mn_2O_3 that has a less protective character than the $MnCr_2O_4$ spinel, which is observed in higher amounts after 24 h. This suggests that the lower oxidation rate obtained initially results from possible Mn volatilization. However, more investigations are needed to explain this apparent increase in the oxidation rate after 24 h.

To discuss the oxide scale composition at 800 °C, thermodynamic calculations were performed using Thermo-Calc software with the TCFE7 database [19,20]. The molar fractions of the various phases *versus* O_2 activity are presented in Fig. 10, where two metallic phases (FCC and BCC) and five oxide structures (M_3O_4 spinel, M_2O_3 corundum, rhodonite, quartz and olivine) are identified. The composition of each phase depending on the O_2 activity has also been calculated but is not presented. In the lowest O_2 activity, the austenitic-FCC phase (*i.e.* steel) is stable and in equilibrium with rhodonite ($MnSiO_3$). According to Fig. 10, for O_2 activity higher than $\sim 10^{-28}$, $MnCr_2O_4$ spinel appears in equilibrium with FCC-austenite and SiO_2, indicating the possibility of internal oxidation. An (Fe,Co)-BCC metallic phase is also stable within the austenitic matrix. For O_2 activity higher than $\sim 10^{-20}$, $(Fe,Mn)_2SiO_4$ olivine and $(Fe,Cr,Mn)_3O_4$ spinel become the major oxide phases. For O_2 activity higher than $\sim 10^{-12}$, FCC-austenite is no longer stable and the external oxide scale is mainly composed of Fe-rich $(Fe,Cr,Mn)_3O_4$ spinel, changing to Fe-rich $(Fe,Cr,Mn)_2O_3$ corundum (in O_2 activities higher than $\sim 10^{-6}$). According to thermodynamic calculations, the oxide scale is composed of spinel at lower O_2 activity and corundum at higher O_2 activity. The structure of the successive layers depending on the O_2 activity are consistent with experimental observations, showing $MnCr_2O_4$ spinel, $(Mn(Cr))_3O_4$ spinel and $(Mn(Cr))_2O_3$ corundum [Figs. 7 and 9(a–b)] from the metal/oxide interface to the oxide/gas interface. Nevertheless, according to elemental mapping (Fig. 7), the oxide scale does not contain Fe.

The absence of Fe occurs because of the high diffusion rate of Mn cations throughout the oxide layer [34], which favor the growth of an Mn oxide layer (Mn_2O_3) on a mixed Mn, Cr and Si oxide layer [35] and result in the formation of Mn-depleted regions at the oxide/metal interface (ferrite) during the oxidation process. However, the Mn_2O_3 layer does not fully cover the alloy surface, as shown by thermodynamic calculations that indicate the presence of a small molar fraction of the alloy (0.06%) in higher O_2 activity. Therefore, new Mn_2O_3 grains nucleate within the voids present in the oxide layer, contributing to an increase in the ferrite layer and a decrease in O_2 activity in the oxide layer which allows for the formation of more stable oxides that require lower O_2 activity, such as $MnCr_2O_4$ and Mn_3O_4 [2,39]. Simultaneously, Mn activity near the oxide/metal interface decreases sharply because of the selective oxidation of this element, which favors Cr oxidation and the formation of $MnCr_2O_4$ at this region [40]. The $MnCr_2O_4$ formation takes place at oxide/metal interface because Mn is

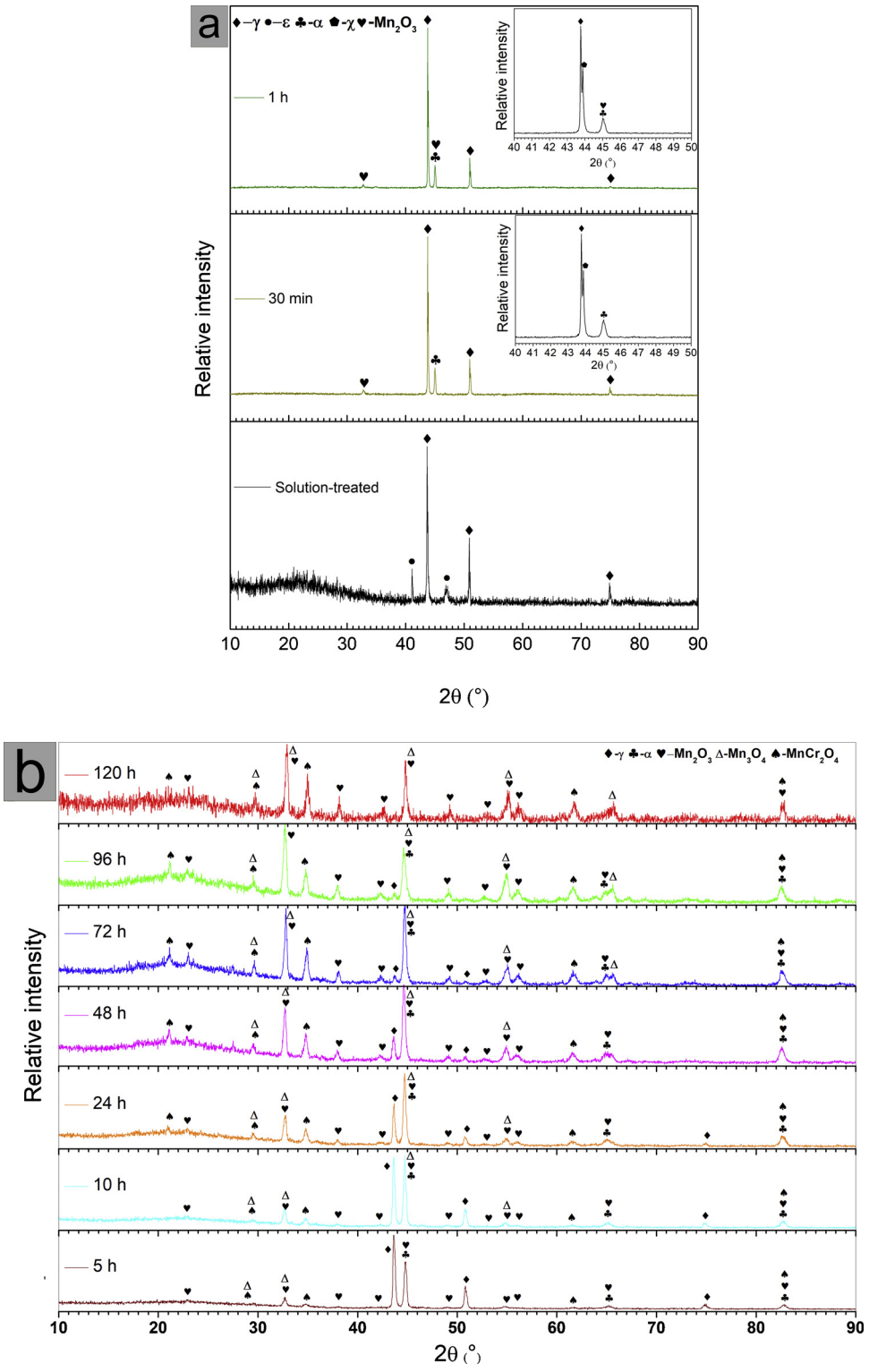

Fig. 9. XRD patterns of the oxides formed on the surfaces of the samples oxidized for 30 min and 1 h (a) and XRD patterns of the oxides formed on the surfaces of the samples oxidized for 5, 10, 24, 48, 72, 96 and 120 h (b).

soluble and possesses a rapid diffusion rate in Cr_2O_3, but a significantly lower diffusion rate in the alloy [41]. On the other hand, the formation of an Mn_3O_4 layer occurs between the outermost layer (Mn_2O_3) and the innermost layer of $MnCr_2O_4$, as a result of the decomposition of Mn_2O_3 and the decrease in O_2 activity within the layer [2,42].

Although the thermodynamic simulations indicate that the formation of a SiO_2 layer can occur, the XRD patterns of the oxide layers formed as a function of oxidation time do not show the presence of SiO_2, which may be a consequence of the SiO_2 layer being amorphous [35]. This fact can be observed by XRD patterns of the oxide layer formed in samples oxidized for up to 120 h [Fig. 9 (b)], which begin to present the formation of an amorphous halo between $20° < 2\theta < 30°$ (and display a loss of sharpness of crystalline peaks in the XRD patterns of this region) as oxidation time increases [43]. Furthermore, the

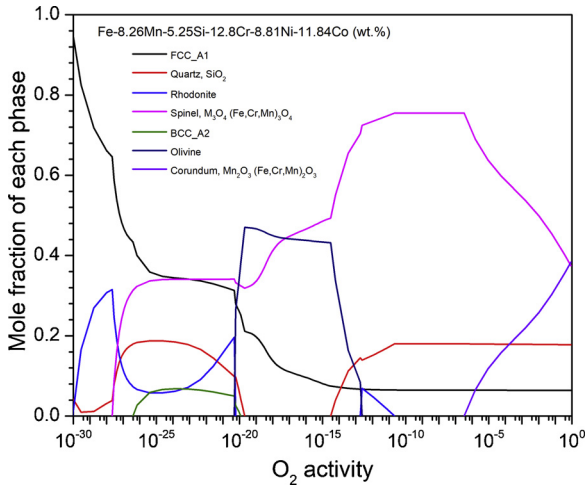

Fig. 10. Calculated mole fraction for each phase in equilibrium of an Fe-8.26Mn-5.25Si-12.8Cr-5.81Ni-11.84Co (wt.%) alloy at 800 °C under various O_2 activities using the Thermo-Calc with the TCFE7 database.

amount of Si present in the alloy matrix may be gradually consumed during the growth of the χ-phase, which contains high Si content and results in the formation of a thinner SiO_2 layer, thus making its detection difficult due to the fact that this layer is formed at the metal/oxide interface. This may also be occurring with Cr as the σ-phase grows, which possibly results in a less protective oxide layer in these regions. However, the weight gain results do not show any abrupt increase in mass gain as a function of the oxidation time.

4. Conclusions

Based on the experimental results, the following conclusions can be drawn:

1 High-temperature exposure for 120 h promotes generalized precipitation of the σ and χ phases inside the metallic matrix grains;
2 The oxidation behavior of Fe-8.26Mn-5.25Si-12.8Cr-8.81Ni-11.84Co SMSS at 800 °C for up to 120 h follows a parabolic law, with the kinetics of oxidation at the initial times of 0–24 h primarily controlled by the growth of the Mn_2O_3 oxide, and after 24 h by the growth of the Mn_3O_4 and $MnCr_2O_4$ spinel;
3 During the oxidation process, the Mn selective oxidation causes a phase transformation from austenite to ferrite in Mn-depleted regions between the base metal and the metal/oxide interface;
4 The present alloy showed an oxidation resistance at least two times greater than FeMnSiCrNi SMSSs previously tested in similar conditions. Even though the behavior of the studied material is not as good as that of a conventional austenitic stainless steel (AISI type 304), the current results indicate that it is an interesting material for coupling pipes that will be used in high temperatures.

Data availability

The raw/processed data required to reproduce these findings cannot be shared at this time due to technical or time limitations.

Acknowledgements

The authors gratefully acknowledge the FAPESP (São Paulo Research Foundation – grant no. 16/10996-4), the PPGCEM/UFSCar (Materials Science and Engineering Postgraduate Program at the Federal University of São Carlos) and the CNPq (National Council for Scientific and Technological Development − grant no. 460659/2014-6 and 311163/2017-3) for their financial support of this work. The use of the facilities at the Monash Centre for Electron Microscopy (MCEM) is also gratefully acknowledged.

References

[1] M. Ghalambaz, M. Abdollahi, A. Eslami, A. Bahrami, A case study on failure of AISI 347H stabilized stainless steel pipe in a petrochemical plant, Case Stud. Eng. Fail. Anal. 9 (2017) 52–62.
[2] R. Ma, H. Peng, Y. Wen, L. Zhang, K. Zhao, Oxidation behavior of an austenitic stainless FeMnSiCrNi shape memory alloy, Corros. Sci. 66 (2013) 269–277.
[3] H.M. Shalaby, Failure investigation of 321 stainless steel pipe to flange weld joint, Eng. Fail. Anal. 80 (2017) 290–298.
[4] C.A. Della Rovere, R. Silva, P. Hammer, J. Otubo, S.E. Kuri, Corrosion behavior of Fe-Mn-Si-Cr-Ni-Co shape memory stainless steel in highly oxidizing medium, Mater. Sci. Forum 869 (2016) 669–674.
[5] H.C. Lin, K.M. Lin, C.S. Lin, T.M. Ouyang, The corrosion behavior of Fe-based shape memory alloys, Corros. Sci. 44 (2002) 2013–2026.
[6] D. Bu, H. Peng, Y. Wen, N. Li, Influence of ageing on wear resistance of an Fe–Mn–Si–Cr–Ni–Ti–C shape memory alloy, Mater. Des. 32 (2011) 2969–2973.
[7] P. Dai, L. Zhou, Investigation on the connecting strength of Fe-Mn-Si-C shape memory alloy pipe coupling, J. Mater. Sci. 41 (2006) 3441–3443.
[8] J.C. Li, X.X. Lü, Q. Jiang, Shape memory effects in an Fe14Mn6Si9Cr5Ni alloy for joining pipe, ISIJ Int. 40 (2000) 1124–1126.
[9] A.M.S. Malafaia, M.F. de Oliveira, Anomalous cyclic oxidation behaviour of a Fe–Mn–Si–Cr–Ni shape memory alloy, Corros. Sci. 119 (2017) 112–117.
[10] V.F. de Souza, A.J. Araújo, J.L.N. Santos, C.A. Della Rovere, A.M.S. Malafaia, Kinetics oxidation and characterization of cyclically oxidized layers at high temperatures for FeMnSiCrNiCe and FeSiCrNi alloys, Mater. Res. 20 (2017) 365–373.
[11] F.H. Stott, F.I. Wei, C.A. Enahoro, The influence of manganese on the High-temperature oxidation of iron-chromium alloys, Mater. Corros. 40 (1989) 198–205.
[12] Q. Gu, J. Van Humbeeck, L. Delaey, A review on the martensitic transformation and shape memory effect in Fe-Mn-Si alloys, J. Phys. 4 (1994) 135–144.
[13] B. Jiang, K. Xu, X. Qi, W. Zhou, Effects of cobalt content on martensitic transformation and shape memory effect in Fe-Mn-Si-Cr-Ni alloys, J. Phys. 112 (2003) 393–396.
[14] R.W. Revie, H.H. Uhlig, Corrosion and Corrosion Control: An Introduction to Corrosion Science and Engineering, fourth edition, (2008).
[15] A.M. Huntz, A. Reckmann, C. Haut, C. Sévérac, M. Herbst, F.C.T. Resende, A.C.S. Sabioni, Oxidation of AISI 304 and AISI 439 stainless steels, Mater. Sci. Eng. A 447 (2007) 266–276.
[16] A.C.S. Sabioni, A.M. Huntz, E.C. da Luz, M. Mantel, C. Haut, Comparative study of high temperature oxidation behaviour in AISI 304 and AISI 439 stainless steels, Mater. Res. 6 (2003) 179–185.
[17] R. Silva, L.F.S. Baroni, C.L. Kugelmeier, M.B.R. Silva, S.E. Kuri, C.A.D. Rovere, Thermal aging at 475 °C of newly developed lean duplex stainless steel 2404: mechanical properties and corrosion behavior, Corros. Sci. 116 (2017) 66–73.
[18] A.F. Padilha, P.R. Rios, Decomposition of austenite in austenitic stainless steels, ISIJ Int. 42 (2002) 325–327.
[19] Thermo-Calc Software AB, TCFE7: TCS Steels/Fe-alloys Database, Version 7.0, Thermo-Calc Software AB, Stockholm, Sweden, 2012.
[20] Thermo-Calc Software AB, Thermo-Calc, Version 4.1, Thermo-Calc Software AB, Stockholm, Sweden, 2014.
[21] S. Kajiwara, Characteristic features of shape memory effect and related transformation behavior in Fe-based alloys, Mater. Sci. Eng. A 273–275 (1999) 67–88.
[22] B.C. Maji, C.M. Das, M. Krishnan, R.K. Ray, The corrosion behaviour of Fe-15Mn-7Si-9Cr-5Ni shape memory alloy, Corros. Sci. 48 (2006) 937–949.
[23] C.A. Della Rovere, J.H. Alano, R. Silva, P.A.P. Nascente, J. Otubo, S.E. Kuri, Characterization of passive films on shape memory stainless steels, Corros. Sci. 57 (2012) 154–161.
[24] V. Fuster, A.V. Druker, A. Baruj, J. Malarría, R. Bolmaro, Characterization of phases in an Fe–Mn–Si–Cr–Ni shape memory alloy processed by different thermo-mechanical methods, Mater. Charact. 109 (2015) 128–137.
[25] Y.H. Wen, H.B. Peng, P.P. Sun, G. Liu, N. Li, A novel training-free cast Fe–18Mn–5.5Si–9.5Cr–4Ni shape memory alloy with lathy delta ferrite, Scr. Mater. 62 (2010) 55–58.
[26] C.A. Della Rovere, M. Castro-Rebello, S.E. Kuri, Corrosion behavior analysis of an austenitic stainless steel exposed to fire, Eng. Fail. Anal. 31 (2013) 40–47.
[27] R. Leiva-García, R. Akid, D. Greenfield, J. Gittens, M.J. Muñoz-Portero, J. García-Antón, Study of the sensitisation of a highly alloyed austenitic stainless steel, Alloy 926 (UNS N08926), by means of scanning electrochemical microscopy, Electrochim. Acta 70 (2012) 105–111.
[28] K.-M. Lin, J.-H. Chen, C.-C. Lin, C.-H. Liu, H.-C. Lin, Optimization of shape-memory effect in Fe-Mn-Si-Cr-Re shape-memory alloys, J. Mater. Eng. Perform. 23 (2014) 2327–2332.
[29] N. Stanford, D.P. Dunne, B.J. Monaghan, Austenite stability in Fe–Mn–Si-based shape memory alloys, J. Alloys Compd. 430 (2007) 107–115.
[30] D.M. Escriba, E. Materna-Morris, R.L. Plaut, A.F. Padilha, Chi-phase precipitation in a duplex stainless steel, Mater. Charact. 60 (2009) 1214–1219.
[31] K.H. Lo, C.H. Shek, J.K.L. Lai, Recent developments in stainless steels, Mater. Sci. Eng. R Rep. 65 (2009) 39–104.
[32] B. Weiss, R. Stickler, Phase instabilities during high temperature exposure of 316 austenitic stainless steel, Metall. Mater. Trans. B 3 (1972) 851–866.
[33] C. Issartel, H. Buscail, E. Caudron, R. Cueff, F. Riffard, S. Perrier, P. Jacquet, M. Lambertin, Influence of nitridation on the oxidation of a 304 steel at 800 °C,

Corros. Sci. 46 (2004) 2191–2201.
[34] R.K. Wild, High temperature oxidation of austenitic stainless steel in low oxygen pressure, Corros. Sci. 17 (1977) 87–104.
[35] G. Coccia Lecis, C. Lenardi, A. Sabatini, The effect of Mn-depleted surface layer on the corrosion resistance of shape memory Fe-Mn-Si-Cr alloys, Metall. Mater. Trans. A 28 (1997) 1219–1222.
[36] K. Hauffe, The mechanism of oxidation of metals and alloys at high temperatures, Prog. Met. Phys. 4 (1953) 71–104.
[37] D.L. Douglass, F. Rizzo-Assuncao, The oxidation of Fe-19.6Cr-15.1Mn stainless steel, Oxid. Met. 29 (1988) 271–287.
[38] D.L. Douglass, F. Gesmundo, C. de Asmundis, The air oxidation of an austenitic Fe-Mn-Cr stainless steel for fusion-reactor applications, Oxid. Met. 25 (1986) 235–268.
[39] A. Col, V. Parry, C. Pascal, Oxidation of a Fe–18Cr–8Ni austenitic stainless steel at 850 °C in O_2: microstructure evolution during breakaway oxidation, Corros. Sci. 114 (2017) 17–27.
[40] R.E. Lobnig, H.P. Schmidt, K. Hennesen, H.J. Grabke, Diffusion of cations in chromia layers grown on iron-base alloys, Oxid. Met. 37 (1992) 81–93.
[41] A. Naoumidis, H.A. Schulze, W. Jungen, P. Lersch, Phase studies in the chromium-manganese-titanium oxide system at different oxygen partial pressures, J. Eur. Ceram. Soc. 7 (1991) 55–63.
[42] A. Šalak, M. Selecká, Thermodynamic conditions for the Mn–O system in sintering of manganese steels, in manganese in powder metallurgy steels, Camb. Int. Sci. (2012) 5–21.
[43] S. Musić, N. Filipović-Vinceković, L. Sekovanić, Precipitation of amorphous SiO_2 particles and their properties, Braz. J. Chem. Eng. 28 (2011) 89–94.